Fracture-Induced Anisotropic Attenuation

José M. Carcione, Juan E. Santos & Stefano Picotti

Rock Mechanics and Rock Engineering

ISSN 0723-2632
Volume 45
Number 5

Rock Mech Rock Eng (2012) 45:929-942
DOI 10.1007/s00603-012-0237-y

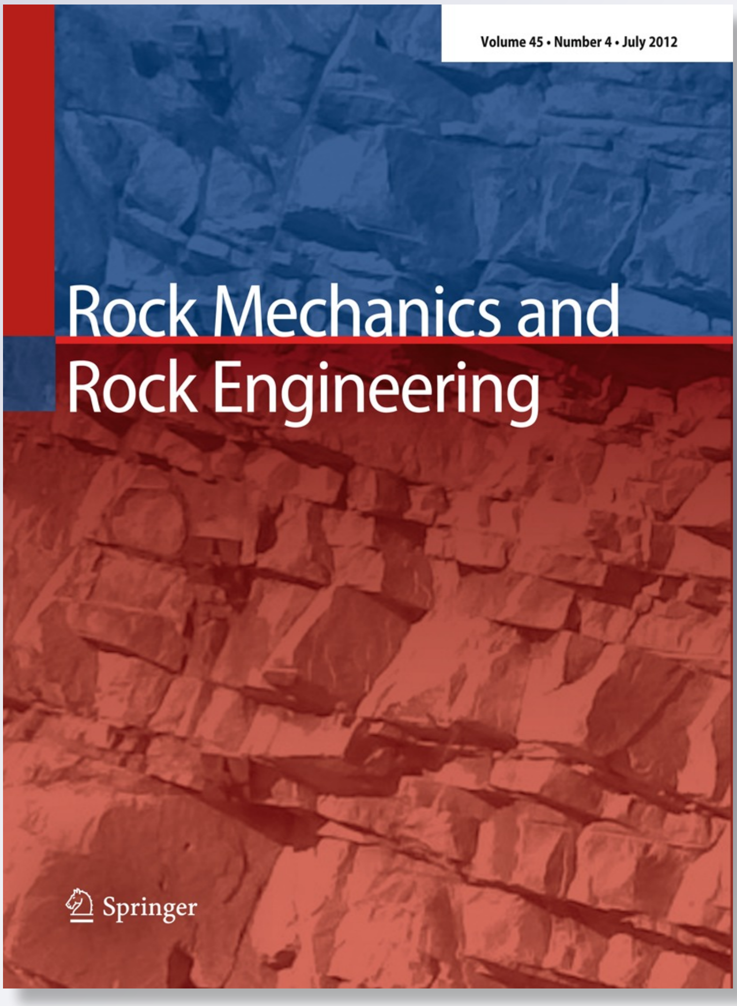

Springer

Rock Mech Rock Eng (2012) 45:929–942
DOI 10.1007/s00603-012-0237-y

ORIGINAL PAPER

Fracture-Induced Anisotropic Attenuation

José M. Carcione · Juan E. Santos · Stefano Picotti

Received: 29 July 2011 / Accepted: 28 February 2012 / Published online: 25 March 2012

Abstract The triaxial nature of the tectonic stress in the earth's crust favors the appearance of vertical fractures. The resulting rheology is usually effective anisotropy with orthorhombic and monoclinic symmetries. In addition, the presence of fluids leads to azimuthally varying attenuation of seismic waves. A dense set of fractures embedded in a background medium enhances anisotropy and rock compliance. Fractures are modeled as boundary discontinuities in the displacement $\mathbf{u}$ and particle velocity $\mathbf{v}$ as $[\boldsymbol{\kappa} \cdot \mathbf{u} + \boldsymbol{\eta} \cdot \mathbf{v}]$, where the brackets denote discontinuities across the fracture surface, $\boldsymbol{\kappa}$ is a fracture stiffness, and $\boldsymbol{\eta}$ is a viscosity related to the energy loss. We consider a transversely isotropic background medium (e.g., thin horizontal plane layers), with sets of long vertical fractures. Schoenberg and Muir's theory combines the background medium and sets of vertical fractures to provide the 13 complex stiffnesses of the long-wavelength equivalent monoclinic and viscoelastic medium. Long-wavelength equivalent means that the dominant wavelength of the signal is much longer than the fracture spacing. The symmetry plane is the horizontal plane. The equations for orthorhombic and transversely isotropic media follow as particular cases. We compute the complex velocities of the medium as a function of frequency and propagation direction, which provide the phase velocities, energy velocities (wavefronts), and quality factors. The effective medium ranges from monoclinic symmetry to hexagonal (transversely isotropic) symmetry from the low- to the high-frequency limits in the case of a particle–velocity discontinuity (lossy case) and the attenuation shows typical Zener relaxation peaks as a function of frequency. The attenuation of the coupled waves may show important differences when computed versus the ray or phase angles, with triplication appearing in the Q factor of the qS wave. We have performed a full-wave simulation to compute the field corresponding to the coupled qP–qS waves in the symmetry plane of an effective monoclinic medium. The simulations agree with the predictions of the plane-wave analysis.

Keywords Fractures · Anisotropy · Attenuation · Schoenberg–Muir theory · Boundary conditions

List of Symbols

$\mathbf{v}$	Particle-velocity vector
$\mathbf{u}$	Displacement vector
ω	Angular frequency
$\mathbf{Z} = (\boldsymbol{\kappa} + i\omega\boldsymbol{\eta})^{-1}$	Fracture compliance matrix
$\boldsymbol{\sigma}$	Stress tensor
e_I, ε_{ij}, $I = 1,\ldots, 6$, $i, j = 1,\ldots, 3$	Strain components
c_{IJ}, $I, J = 1,\ldots, 6$	Elasticity components

J. M. Carcione (✉) · S. Picotti
Istituto Nazionale di Oceanografia e di Geofisica Sperimentale
(OGS), Borgo Grotta Gigante 42c, 34010 Sgonico, Trieste, Italy
e-mail: jcarcione@inogs.it

J. E. Santos
CONICET, Instituto del Gas y del Petróleo,
Facultad de Ingeniería, Universidad de Buenos Aires,
C1127AAR Buenos Aires, Argentina
e-mail: santos@math.purdue.edu

J. E. Santos
Universidad Nacional de La Plata, La Plata, Argentina

J. E. Santos
Department of Mathematics, Purdue University,
W. Lafayette, IN 47907-2067, USA

s_{IJ}, I, $J = 1, \ldots, 6$	Compliance components
β	Angle between the fracture plane and the y-axis
$\mathbf{P}$	Stiffness tensor
ρ	Mass density
λ, μ, $E = \lambda + 2\mu$	Lamé constants
$\mathbf{\Gamma}$	Kelvin–Christoffel matrix
v_p	Phase velocity
Q	Quality factor
v_e	Energy velocity
θ	Phase velocity angle
ψ	Energy-velocity angle

1 Introduction

Wave propagation through fractures, faults, and cracks is an important subject in seismology, exploration geophysics, and mining. Faults in the earth's crust constitute sources of earthquakes (Pyrak-Nolte et al. 1990) and hydrocarbon and geothermal reservoirs are mainly composed of fractured rocks (Nakagawa and Myer 2009). Applications in geotechnical engineering, such as analysis of the dynamic stability of rock slopes and tunnels, involve the study of imperfect joints in rock masses (Perino et al. 2010; Fan et al. 2011). In geophysical prospecting, knowledge of reservoirs' fracture orientations, densities, and sizes is essential, since these factors control hydrocarbon production (Hansen 2002; Hall and Kendall 2003; Grechka and Tsvankin 2003; Barton 2007). The analysis of the data exploits the fact that seismic velocity and attenuation anisotropy due to the presence of fractures are sensitive to key properties of the reservoir, such as porosity, permeability, and fluid type.

A few frequency-dependent models have been developed to describe anisotropy and attenuation. Carcione (1992) generalized Backus averaging to the anelastic case, obtaining the first model for Q-anisotropy (see Carcione 2007). Analyses on sequences of sandstone–limestone and shale–limestone with different degrees of anisotropy indicate that the quality factors (Q) of the shear modes are more anisotropic than the corresponding phase velocities, cusps of the qSV mode are more pronounced for low frequencies and midrange proportions, and, in general, attenuation is higher in the direction perpendicular to layering or close to it, provided that the material with lower velocity is the more dissipative. This model has been further analyzed by Picotti et al. (2010), who shown how to obtain the medium properties with quasi-static numerical experiments. Other alternative models of Q-anisotropy were proposed by Carcione and Cavallini (1994) and Carcione et al. (1998). A brief description of all these phenomenological models can be found in Carcione (2007). Zhu and Tsvankin (2007) analyze in detail the attenuation in orthorhombic media, assuming homogeneous viscoelastic waves. They simplify the interpretation for processing purposes by introducing a set of attenuation anisotropy parameters. A Backus type model to describe wave propagation in fractures has been introduced by Carcione (1996a), where plane layers are separated by thin continuous layers of viscous fluid. A similar model is considered by Liu et al. (2000), where the fracture is a very thin soft viscous layer.

On the other hand, a recently developed model (Chapman 2003; Maultzsch 2005) explicitly describes the effects of cracks and fractures on wave propagation, since the elastic constants are derived in terms of microstructural parameters and, therefore, the model is predictive. It describes attenuation and velocity dispersion at seismic frequencies and predicts how these effects are related to the fluid type and size of the fractures. An approach to explicitly model cracks and fractures is proposed by Zhang and Gao (2009). Their scheme treats the fractures as non-welded interfaces that satisfy the linear-slip displacement discontinuity conditions instead of using equivalent medium theories. Hence, the algorithm can be used to characterize the seismic response of fractured media and to test equivalent medium theories. Other poroelasticity models describing anisotropic attenuation are given by Krzikalla and Müller (2011) and Carcione et al. (2011), who obtain the five complex and frequency-dependent stiffnesses of an equivalent medium corresponding to thin poroelastic layers.

Modeling fractures requires a suitable interface model for describing the dynamic response of the joint. Theories that consider imperfect contact were mainly based on the displacement discontinuity model at the interface. Pyrak-Nolte et al. (1990) proposed a non-welded interface model based on the discontinuity of the displacement and the particle velocity across the interface. The stress components are proportional to the displacement and velocity discontinuities through the specific stiffnesses and one specific viscosity, respectively. Displacement discontinuities conserve energy and yield frequency-dependent reflection and transmission coefficients. On the other hand, velocity discontinuities generate energy loss at the interface. The specific viscosity accounts for the presence of a liquid under saturated conditions. The liquid introduces a viscous coupling between the two surfaces of the fracture (Schoenberg 1980) and enhances energy transmission, but, at the same time, this is reduced by viscous losses. The model may account for slip and dilatancy effects. Chichinina et al. (2009a, b) describe anisotropic attenuation in a transversely isotropic (TI) medium using Schoenberg's linear-slip model with complex-valued normal and tangential fracture stiffnesses. The theory and laboratory experiments show that, in the vicinity of the symmetry axis, P-wave attenuation is comparable to S-wave attenuation when the fracture is filled with a fluid. On the other hand, in the presence of dry fractures, P-wave attenuation is much greater than S-wave attenuation.

In this work, we generalize the orthorhombic model given by Schoenberg and Helbig (1997) to the anelastic monoclinic case, by introducing a particle-velocity discontinuity in the fracture surface, allowing us to describe Q-anisotropy. The medium consists of sets of vertical fractures embedded in a TI background medium (generally, horizontal fine layering) to form a long-wavelength equivalent monoclinic medium. Using the theory of Schoenberg and Muir (1989), we obtain the 13 complex and frequency-dependent stiffnesses of this medium. We then obtain the quality factors and wave velocities as a function of frequency and propagation angle.

2 Interface Model

Let us consider a planar fracture. The non-ideal characteristics of the interface are modeled by imposing suitable boundary conditions. The model proposed here is based on the discontinuity of the displacement and particle-velocity fields across the interface. Then, the boundary conditions at the interface are

$$\boldsymbol{\kappa} \cdot [\mathbf{u}] + \boldsymbol{\eta} \cdot [\mathbf{v}] = \boldsymbol{\sigma} \cdot \mathbf{n}, \tag{1}$$

(Pyrak-Nolte et al. 1990; Carcione 1996b), where $\mathbf{u}$ and $\mathbf{v}$ are the displacement and particle-velocity components, respectively, $\boldsymbol{\sigma}$ is the 3×3 stress tensor, $\mathbf{n}$ is the unit normal to the fracture, $\boldsymbol{\kappa}$ is the specific stiffness matrix, and $\boldsymbol{\eta}$ is the specific viscosity matrix (both of dimensions 3×3). They have dimensions of stiffness and viscosity per unit length, respectively. Moreover, the symbol "$\cdot$" indicates scalar product and the brackets denote discontinuities across the interface, such that for a field variable ϕ, it is $[\phi] = \phi_2 - \phi_1$, where 1 and 2 indicate the two sides of the fracture.

The particle velocity is given by

$$\mathbf{v} = \dot{\mathbf{u}}, \tag{2}$$

where a dot above a variable indicates time differentiation. In the Fourier domain,

$$\mathbf{v} = i\omega\mathbf{u}, \tag{3}$$

where ω is the angular frequency and $i = \sqrt{-1}$. Equation (1) then becomes

$$[\mathbf{u}] = \mathbf{Z} \cdot (\boldsymbol{\sigma} \cdot \mathbf{n}), \tag{4}$$

where

$$\mathbf{Z} = (\boldsymbol{\kappa} + i\omega\boldsymbol{\eta})^{-1} \tag{5}$$

is a fracture compliance matrix, whose dimension is length/stress. This approach is equivalent to the linear-slip model introduced by Schoenberg (1980). In fact, Eq. (5), with $\boldsymbol{\eta} = 0$, is given in Coates and Schoenberg (1995) and Schoenberg and Helbig (1997). Three models have been studied by Liu et al. (2000) to obtain the expression of $\mathbf{Z}$ for different fracture models. Two of the models only provide the real part of $\mathbf{Z}$. The third model describes the fracture as a thin and soft viscoelastic layer embedded in an isotropic elastic background medium, where $\mathbf{Z}$ can be obtained in terms of the thickness, Lamé constants, and viscosity of the soft material infill. The resulting equivalent medium has TI symmetry. Similarly, Carcione (1996a) described the infill by a viscous fluid.

The compliance matrix $\mathbf{Z}$ of the set of fractures is the diagonal non-negative matrix

$$\mathbf{Z} = \begin{pmatrix} Z_1 & 0 & 0 \\ 0 & Z_2 & 0 \\ 0 & 0 & Z_3 \end{pmatrix} = \begin{pmatrix} (\kappa_1 + i\omega\eta_1)^{-1} & 0 & 0 \\ 0 & (\kappa_2 + i\omega\eta_2)^{-1} & 0 \\ 0 & 0 & (\kappa_3 + i\omega\eta_3)^{-1} \end{pmatrix}, \tag{6}$$

where Z_1 is the normal compliance, Z_2 is the horizontal tangential compliance, and Z_3 is the vertical tangential compliance. The fact that $Z_2 \neq Z_3$ means that the texture of the fracture surface has different roughnesses vertically and horizontally, while the fact that there are no off-diagonal components means that, across the fractures, the normal motion is uncoupled from the tangential motion.

A common situation in the earth's crust is to have a finely layered medium and vertical fractures. Figure 1 shows such a case, where $q = 2$ sets of long vertical fractures are embedded in a TI medium with a vertical symmetry. This background medium is the long-wavelength equivalent of the finely layered medium, according to Backus (1962). The mechanical (viscoelastic) representation of the fracture boundary condition by a Kelvin–Voigt model is illustrated in the figure, according to the stress-displacement relation

$$\boldsymbol{\sigma} \cdot \mathbf{n} = (\boldsymbol{\kappa} + i\omega\boldsymbol{\eta}) \cdot [\mathbf{u}], \tag{7}$$

where the model simulates the fracture by a zero-width layer of distributed springs and dashpots. The quantity $\boldsymbol{\kappa} + i\omega\boldsymbol{\eta}$ is the complex modulus per unit length of the Kelvin–Voigt element (e.g., Carcione 2007).

A displacement discontinuity yields compliance, while a discontinuity in the particle velocity implies an energy loss at

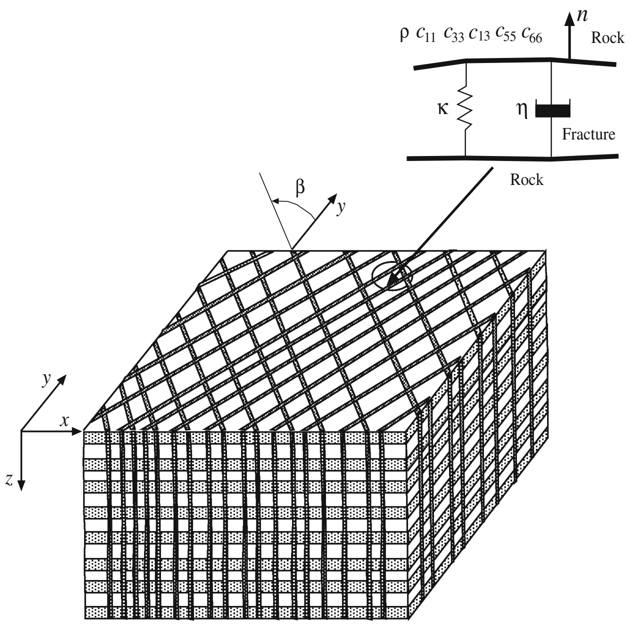

Fig. 1 Two sets of vertical fractures embedded in a transversely isotropic (TI) medium. In this case, transverse isotropy is due to fine layering. If the two sets are orthogonal, the equivalent medium is orthorhombic; otherwise, the symmetry is monoclinic with a horizontal single plane of symmetry. The boundary condition at the fracture describes an imperfect bonding in terms of the specific stiffness $\boldsymbol{\kappa}$ and specific viscosity $\boldsymbol{\eta}$. Angle β is measured from the y-axis towards the strike direction

the interface (Carcione et al. 1996b, 1998, 2007); $\boldsymbol{\kappa} = 0$ gives the particle-velocity discontinuity model and $\boldsymbol{\eta} = 0$ gives the displacement discontinuity model. On the other hand, if $\boldsymbol{\kappa} \to \infty$ or $\boldsymbol{\eta} \to \infty$, the model gives a welded interface.

2.1 The Equivalent Monoclinic Medium

Let us consider a background TI medium. The stress–strain relation is

$$\begin{pmatrix}\sigma_1\\ \sigma_2\\ \sigma_3\\ \sigma_4\\ \sigma_5\\ \sigma_6\end{pmatrix} = \begin{pmatrix}\sigma_{11}\\ \sigma_{22}\\ \sigma_{33}\\ \sigma_{23}\\ \sigma_{13}\\ \sigma_{12}\end{pmatrix} = \begin{pmatrix} c_{11} & c_{12} & c_{13} & 0 & 0 & 0\\ c_{12} & c_{11} & c_{13} & 0 & 0 & 0\\ c_{13} & c_{13} & c_{33} & 0 & 0 & 0\\ 0 & 0 & 0 & c_{55} & 0 & 0\\ 0 & 0 & 0 & 0 & c_{55} & 0\\ 0 & 0 & 0 & 0 & 0 & c_{66}\end{pmatrix} \begin{pmatrix}e_1\\ e_2\\ e_3\\ e_4\\ e_5\\ e_6\end{pmatrix} \equiv \mathbf{C} \begin{pmatrix}e_1\\ e_2\\ e_3\\ e_4\\ e_5\\ e_6\end{pmatrix}, \tag{8}$$

where

$$2c_{66} = c_{11} - c_{12},$$

σ_I denotes the stress component and e_I denotes the strain component in the Voigt notation (e.g., Carcione 2007), such that

$$[e_1, e_2, e_3, e_4, e_5, e_6]^\top = [\epsilon_{11}, \epsilon_{22}, \epsilon_{33}, 2\epsilon_{23}, 2\epsilon_{13}, 2\epsilon_{12}]^\top, \tag{9}$$

where ϵ_{ij} are the strain components, c_{IJ} are the elasticity constants, and $\mathbf{C}$ is the elasticity matrix.

The background medium can easily be generalized to a viscoelastic medium by using one of the three models of anisotropic anelasticity proposed in Chapter 4 of Carcione (2007). The generalization implies that the elasticity constants c_{IJ} become complex and frequency dependent. Here, the purpose is to analyze the attenuation due to the fracture solely; however, in the last example, we consider an effective HTI (TI with a horizontal symmetry axis) medium to test the commonly used equation by which the total dissipation factor is equal to the dissipation factor of the background medium plus the dissipation factor due to the fractures.

Schoenberg and Muir (1989) showed how to combine arbitrary sets of elastic thin layers and find their long-wavelength equivalent medium properties. The method is applicable also when a set of layers is infinitely thin and compliant, as it is the fracture set shown in Fig. 1. Nichols et al. (1989) and Hood (1991) simplified the procedure to include fractures by using compliance matrices instead of stiffness matrices. As shown below, the compliance matrix of the equivalent medium is found by the addition of expanded 6 × 6 versions of the fracture compliance matrices to the compliance matrix of the background medium.

Let us consider many sets of vertical fractures, so that the fracture normal of a given set makes an angle β with the x-axis (see Fig. 1). We avoid the fracture index (q) for simplicity. The expanded fracture compliance matrix of each set is

$$\mathbf{S}_f = \begin{pmatrix} s_{11} & s_{12} & 0 & 0 & 0 & s_{16}\\ s_{12} & s_{22} & 0 & 0 & 0 & s_{26}\\ 0 & 0 & 0 & 0 & 0 & 0\\ 0 & 0 & 0 & s_{44} & s_{45} & 0\\ 0 & 0 & 0 & s_{45} & s_{55} & 0\\ s_{16} & s_{26} & 0 & 0 & 0 & s_{66}\end{pmatrix}, \tag{10}$$

where

$$\begin{aligned}
s_{11} &= \frac{3Z_N + Z_H}{8} + \frac{Z_N}{2}\cos 2\beta + \frac{Z_N - Z_H}{8}\cos 4\beta,\\
s_{12} &= \frac{Z_N - Z_H}{8}(1 - \cos 4\beta),\\
s_{16} &= \frac{Z_N \sin 2\beta}{2} + \frac{Z_N - Z_H}{4}\sin 4\beta,\\
s_{22} &= \frac{3Z_N + Z_H}{8} - \frac{Z_N}{2}\cos 2\beta + \frac{Z_N - Z_H}{8}\cos 4\beta,\\
s_{26} &= \frac{Z_N \sin 2\beta}{2} - \frac{Z_N - Z_H}{4}\sin 4\beta,\\
s_{44} &= \frac{Z_V(1 - \cos 2\beta)}{2},\\
s_{45} &= \frac{Z_V \sin 2\beta}{2},\\
s_{55} &= \frac{Z_V(1 + \cos 2\beta)}{2},\\
s_{66} &= \frac{Z_N + Z_H}{2} - \frac{Z_N - Z_H}{2}\cos 4\beta
\end{aligned} \tag{11}$$

(Schoenberg et al. 1999). The computation of the compliance matrix in Eq. (10) can be derived by carrying out the matrix multiplication given by Nichols et al. (1989) or directly using 4th-rank tensor notation.

We have introduced

$$Z_N = \frac{Z_1}{L},\ Z_H = \frac{Z_2}{L},\ Z_V = \frac{Z_3}{L}, \tag{12}$$

where L is a characteristic length, such that these quantities have dimensions of compliance, and

$$\begin{aligned}
&\kappa_N = L\kappa_1,\ \kappa_H = L\kappa_2,\ \kappa_V = L\kappa_3,\\
&\eta_N = L\eta_1,\ \eta_H = L\eta_2,\ \eta_V = L\eta_3,
\end{aligned} \tag{13}$$

such that these quantities have dimensions of stiffness and viscosity, respectively. The quantity L, called h in Grechka et al. (2003) (see their Eq. 3), is the average fracture spacing, which has to be much smaller than the dominant wavelength of the pulse.

It is

$$Z_N = \frac{1}{\kappa_N + i\omega\eta_N},\ Z_H = \frac{1}{\kappa_H + i\omega\eta_H},\ Z_V = \frac{1}{\kappa_V + i\omega\eta_V}. \tag{14}$$

Then, the complex and frequency-dependent stiffness matrix of the equivalent medium is given by

$$\mathbf{P}(\omega) = \left[\mathbf{C}^{-1} + \sum_q \mathbf{S}_f^{(q)}(\omega)\right]^{-1}, \tag{15}$$

where the sum is over the q sets of fractures. The equivalent homogeneous anisotropic medium (in the long wavelength limit) is a monoclinic medium with a horizontal mirror plane of symmetry. Its complex and frequency-dependent stiffness matrix has the form

$$\mathbf{P} = \begin{pmatrix}
p_{11} & p_{12} & p_{13} & 0 & 0 & p_{16}\\
p_{12} & p_{22} & p_{23} & 0 & 0 & p_{26}\\
p_{13} & p_{23} & p_{33} & 0 & 0 & p_{36}\\
0 & 0 & 0 & p_{44} & p_{45} & 0\\
0 & 0 & 0 & p_{45} & p_{55} & 0\\
p_{16} & p_{26} & p_{36} & 0 & 0 & p_{66}
\end{pmatrix}. \tag{16}$$

At zero frequency, we obtain the lossless case, where $Z_N = 1/\kappa_N$, $Z_H = 1/\kappa_H$, and $Z_V = 1/\kappa_V$, and the medium remains monoclinic. At "infinite" frequency, the fracture stiffnesses vanish ($\mathbf{S}_f^{(q)} \to 0$) and we obtain the TI and lossless background medium. By "infinite" frequency, we mean frequencies such that the wavelength is much larger than the distance between single fractures, i.e., the long-wavelength approximation. It can be shown that the wave velocities at zero frequency are smaller than the wave velocities at infinite frequency, i.e., the medium is more compliant.

2.2 Orthorhombic Equivalent Media

Assume two fracture sets with $\beta = 0$ (fracture strike along the y-direction) and $\beta = \pi/2$ (fracture strike points along the x-direction). The fracture stiffness matrices are given by

$$\mathbf{S}_f^{(1)} = \begin{pmatrix}
Z_N^{(1)} & 0 & 0 & 0 & 0 & 0\\
0 & 0 & 0 & 0 & 0 & 0\\
0 & 0 & 0 & 0 & 0 & 0\\
0 & 0 & 0 & 0 & 0 & 0\\
0 & 0 & 0 & 0 & Z_V^{(1)} & 0\\
0 & 0 & 0 & 0 & 0 & Z_H^{(1)}
\end{pmatrix} \tag{17}$$

and

$$\mathbf{S}_f^{(2)} = \begin{pmatrix}
0 & 0 & 0 & 0 & 0 & 0\\
0 & Z_N^{(2)} & 0 & 0 & 0 & 0\\
0 & 0 & 0 & 0 & 0 & 0\\
0 & 0 & 0 & Z_V^{(2)} & 0 & 0\\
0 & 0 & 0 & 0 & 0 & 0\\
0 & 0 & 0 & 0 & 0 & Z_H^{(2)}
\end{pmatrix}, \tag{18}$$

respectively.

The evaluation of Eq. (15) requires simple operations with 3 × 3 matrices. We obtain

$$
\begin{aligned}
p_{11} &= \frac{c_{11} + Z_N^{(2)}(c_{11}^2 - c_{12}^2)}{1 + Z_N^{(1)} Z_N^{(2)}(c_{11}^2 - c_{12}^2) + c_{11}(Z_N^{(1)} + Z_N^{(2)})}, \\
p_{12} &= \frac{c_{12}}{1 + Z_N^{(1)} Z_N^{(2)}(c_{11}^2 - c_{12}^2) + c_{11}(Z_N^{(1)} + Z_N^{(2)})}, \\
p_{13} &= \frac{c_{13}[1 + Z_N^{(2)}(c_{11} - c_{12})]}{1 + Z_N^{(1)} Z_N^{(2)}(c_{11}^2 - c_{12}^2) + c_{11}(Z_N^{(1)} + Z_N^{(2)})}, \\
p_{22} &= \frac{c_{11} + Z_N^{(1)}(c_{11}^2 - c_{12}^2)}{1 + Z_N^{(1)} Z_N^{(2)}(c_{11}^2 - c_{12}^2) + c_{11}(Z_N^{(1)} + Z_N^{(2)})}, \\
p_{23} &= \frac{c_{13}[1 + Z_N^{(1)}(c_{11} - c_{12})]}{1 + Z_N^{(1)} Z_N^{(2)}(c_{11}^2 - c_{12}^2) + c_{11}(Z_N^{(1)} + Z_N^{(2)})}, \\
p_{33} &= \frac{c_{33} + (Z_N^{(1)} + Z_N^{(2)})(c_{11}c_{33} - c_{13}^2) + Z_N^{(1)} Z_N^{(2)}(c_{11} - c_{12})[c_{33}(c_{11} + c_{12}) - 2c_{13}^2]}{1 + Z_N^{(1)} Z_N^{(2)}(c_{11}^2 - c_{12}^2) + c_{11}(Z_N^{(1)} + Z_N^{(2)})}, \\
p_{44} &= \frac{c_{55}}{1 + c_{55} Z_V^{(2)}}, \\
p_{55} &= \frac{c_{55}}{1 + c_{55} Z_V^{(1)}}, \\
p_{66} &= \frac{c_{66}}{1 + c_{66}(Z_H^{(1)} + Z_H^{(2)})}.
\end{aligned}
\tag{19}
$$

Since the two sets are orthogonal, the equivalent medium has orthorhombic symmetry. In the case of a single fracture set, e.g., $\beta = 0$, Eq. (19) gives the stiffness matrix of Schoenberg and Helbig (1997):

$$
\mathbf{P} = \begin{pmatrix}
c_{11}(1-\delta_N) & c_{12}(1-\delta_N) & c_{13}(1-\delta_N) & 0 & 0 & 0 \\
c_{12}(1-\delta_N) & c_{11}(1-\delta_N c_{12}^2/c_{11}^2) & c_{13}(1-\delta_N c_{12}/c_{11}) & 0 & 0 & 0 \\
c_{13}(1-\delta_N) & c_{13}(1-\delta_N c_{12}/c_{11}) & c_{33}[1-\delta_N c_{13}^2/(c_{11}c_{33})] & 0 & 0 & 0 \\
0 & 0 & 0 & c_{55} & 0 & 0 \\
0 & 0 & 0 & 0 & c_{55}(1-\delta_V) & 0 \\
0 & 0 & 0 & 0 & 0 & c_{66}(1-\delta_H)
\end{pmatrix},
\tag{20}
$$

where

$$
\delta_N = [1 + 1/(Z_N c_{11})]^{-1}, \; \delta_H = [1 + 1/(Z_H c_{66})]^{-1}, \quad \delta_V = [1 + 1/(Z_V c_{55})]^{-1}. \tag{21}
$$

2.3 HTI Equivalent Media

If the background medium is isotropic ($c_{11} = c_{12} + 2c_{55}, c_{12} = c_{13}, c_{55} = c_{66}$) and the fracture set is rotationally invariant, we have $Z_H = Z_V \equiv Z_T$, and the equivalent medium is TI with a horizontal symmetry axis (HTI), whose stiffness matrix is

$$
\mathbf{P} = \begin{pmatrix}
c_{11}c_N & c_{12}c_N & c_{12}c_N & 0 & 0 & 0 \\
c_{12}c_N & c_{11} - c_{12}^2 Z_N c_N & c_{12} - c_{12}^2 Z_N c_N & 0 & 0 & 0 \\
c_{12}c_N & c_{12} - c_{12}^2 Z_N c_N & c_{11} - c_{12}^2 Z_N c_N & 0 & 0 & 0 \\
0 & 0 & 0 & c_{55} & 0 & 0 \\
0 & 0 & 0 & 0 & c_{55}c_T & 0 \\
0 & 0 & 0 & 0 & 0 & c_{55}c_T
\end{pmatrix},
\tag{22}
$$

where

$$c_N = (1 + c_{11}Z_N)^{-1} \text{ and } c_T = (1 + c_{55}Z_T)^{-1}. \tag{23}$$

The stiffness matrix in Coates and Schoenberg (1995) is equivalent to Eq. (22) with a rotation of $\pi/2$ around the y-axis and considering the lossless case ($\boldsymbol{\eta} = 0$). If $\boldsymbol{\eta} \neq 0$, Eq. (22) is equivalent to the medium studied by Chichinina et al. (2009b).

The fractured medium defined by Eq. (22) can be obtained from Backus averaging (Backus 1962) of a periodic medium composed of two isotropic constituents with proportions p_i, and P-wave and S-wave moduli, respectively, given by E_i and $\mu_i, i = 1, 2$. Backus' effective stiffness constants are given by (Carcione 2007)

$$\begin{aligned}
p_{11} &= [E_1E_2 + 4p_1p_2(\mu_1 - \mu_2)(\lambda_1 + \mu_1 - \lambda_2 - \mu_2)]D,\\
p_{12} &= [\lambda_1\lambda_2 + 2(\lambda_1p_1 + \lambda_2p_2)(\mu_2p_1 + \mu_1p_2)]D,\\
p_{13} &= (\lambda_1p_1E_2 + \lambda_2p_2E_1)D\\
p_{33} &= E_1E_2D,\\
p_{55} &= \mu_1\mu_2(p_1\mu_2 + p_2\mu_1)^{-1},\\
p_{66} &= p_1\mu_1 + p_2\mu_2,\\
D &= (p_1E_2 + p_2E_1)^{-1}.
\end{aligned} \tag{24}$$

Equation (22) is then obtained by taking the limits $p_1 \to 1$ and $p_2 \to 0$ (or $p_2 \ll p_1$) and setting $E_1 = c_{11}$ and $\mu_1 = c_{55}$ (background medium) and $E_2 = p_2/Z_N$ and $\mu_2 = p_2/Z_H$ (fracture). This is shown by Schoenberg (1983) in the lossless case.

3 Properties of the Effective Medium

A general plane-wave solution for the displacement field $\mathbf{u} = (u_x, u_y, u_z)^\top = (u_1, u_2, u_3)^\top$ is

$$\mathbf{u} = \mathbf{U}\exp[i\omega(t - s_1x - s_2y - s_3z)], \tag{25}$$

where s_i are the components of the slowness vector $\mathbf{s} = (s_1, s_2, s_3)$, $\mathbf{U}$ is a complex vector, and t is the time variable. We consider homogeneous viscoelastic waves, such that $\mathbf{s} = s(l_1, l_2, l_3)$, where $s = \sqrt{s_1^2 + s_2^2 + s_3^2}$, and l_i are the direction cosines defining the propagation (and attenuation) directions. The complex velocity is

$$v = \frac{1}{s}. \tag{26}$$

3.1 Symmetry Plane of a Monoclinic Medium

In the symmetry plane of a monoclinic medium, there is a pure shear wave and two coupled waves. The respective dispersion relations in the (x, y)-plane are

$$\begin{aligned}
&\Gamma_{33} - \rho v^2 = 0,\\
&(\Gamma_{11} - \rho v^2)(\Gamma_{22} - \rho v^2) - \Gamma_{12}^2 = 0,
\end{aligned} \tag{27}$$

where ρ is the density of the background medium,

$$\begin{aligned}
\Gamma_{11} &= p_{11}l_1^2 + p_{66}l_2^2 + 2p_{16}l_1l_2,\\
\Gamma_{22} &= p_{66}l_1^2 + p_{22}l_2^2 + 2p_{26}l_1l_2,\\
\Gamma_{33} &= p_{55}l_1^2 + p_{44}l_2^2 + 2p_{45}l_1l_2,\\
\Gamma_{12} &= p_{16}l_1^2 + p_{26}l_2^2 + (p_{12} + p_{66})l_1l_2,
\end{aligned} \tag{28}$$

(Carcione 2007), where v is the complex velocity and $l_1 = \sin\theta$ and $l_2 = \cos\theta$, with θ being the phase propagation angle.

If we label 1 the pure mode (the SH wave) and 2 and 3 the qS and qP waves, the corresponding complex velocities are (e.g., Carcione 2007)

$$\begin{aligned}
v_1 &= \sqrt{\rho^{-1}(p_{55}l_1^2 + p_{44}l_2^2 + 2p_{45}l_1l_2)},\\
v_2 &= (2\rho)^{-1/2}\sqrt{p_{11}l_1^2 + p_{22}l_2^2 + p_{66} + 2l_1l_2(p_{16} + p_{26}) - A},\\
v_3 &= (2\rho)^{-1/2}\sqrt{p_{11}l_1^2 + p_{22}l_2^2 + p_{66} + 2l_1l_2(p_{16} + p_{26}) + A},\\
A &= \sqrt{(\Gamma_{11} - \Gamma_{22})^2 + 4\Gamma_{12}^2}.
\end{aligned} \tag{29}$$

The phase velocity is given by

$$v_\mathrm{p} = \left[\mathrm{Re}\left(\frac{1}{v}\right)\right]^{-1} \tag{30}$$

and the quality factor is simply

$$Q = \frac{\mathrm{Re}(v^2)}{\mathrm{Im}(v^2)} \tag{31}$$

(e.g., Carcione 2007). The values of the qP quality factor along orthogonal directions are

$$Q_\mathrm{P}(\theta = \pi/2) = \frac{\mathrm{Re}(p_{11})}{\mathrm{Im}(p_{11})} \text{ and } Q_\mathrm{P}(\theta = 0) = \frac{\mathrm{Re}(p_{22})}{\mathrm{Im}(p_{22})}, \tag{32}$$

respectively, while those of the shear waves are

$$\begin{aligned}
&Q_{SV}(\theta = \pi/2) = Q_{SV}(\theta = 0) = Q_\mathrm{SH}(\theta = 0) = \frac{\mathrm{Re}(p_{44})}{\mathrm{Im}(p_{44})},\\
&\text{and } Q_\mathrm{SH}(\theta = \pi/2) = \frac{\mathrm{Re}(p_{55})}{\mathrm{Im}(p_{55})}.
\end{aligned} \tag{33}$$

Next, we obtain the energy velocity at zero frequency (the lossless elastic limit) times one unit of time. The SH wave energy velocity is

$$\mathbf{v}_\mathrm{e} = \frac{1}{\rho v_\mathrm{p}}[(c_{55}^0l_1 + c_{45}^0l_2)\hat{\mathbf{e}}_1 + (c_{44}^0l_2 + c_{45}^0l_1)\hat{\mathbf{e}}_2]. \tag{34}$$

On the other hand, the qP and qS energy-velocity components v_{e1} and v_{e2} are

$$\begin{aligned}&\rho v_{\mathrm{p}}(\Gamma_{11}+\Gamma_{22}-2\rho v_{\mathrm{p}}^2)v_{\mathrm{e}1}\\ &=(\Gamma_{22}-\rho v_{\mathrm{p}}^2)(c_{11}^0 l_1+c_{16}^0 l_2)\\ &\quad+(\Gamma_{11}-\rho v_{\mathrm{p}}^2)(c_{66}^0 l_1+c_{26}^0 l_2)\\ &\quad-\Gamma_{12}[2c_{16}^0 l_1+(c_{12}^0+c_{66}^0)l_2]\end{aligned} \tag{35}$$

and

$$\begin{aligned}&\rho v_{\mathrm{p}}(\Gamma_{11}+\Gamma_{22}-2\rho v_{\mathrm{p}}^2)v_{\mathrm{e}2}\\ &=(\Gamma_{22}-\rho v_{\mathrm{p}}^2)(c_{66}^0 l_2+c_{16}^0 l_1)\\ &\quad+(\Gamma_{11}-\rho v_{\mathrm{p}}^2)(c_{22}^0 l_2+c_{26}^0 l_1)\\ &\quad-\Gamma_{12}[2c_{26}^0 l_2+(c_{12}^0+c_{66}^0)l_1],\end{aligned} \tag{36}$$

where c_{IJ}^0 are the zero-frequency limits of the p_{IJ} (e.g., Carcione 2007).

3.2 Orthorhombic Media

The dispersion relation has the same form as in the lossless case, but replacing the (real) elasticity constants by the complex stiffnesses p_{IJ}, i.e., the components of matrix $\mathbf{P}$. Following Schoenberg and Helbig (1997), we have

$$v^6-a_2v^4+a_1v^2-a_0=0, \tag{37}$$

where

$$\begin{aligned}a_0&=\Gamma_{11}\Gamma_{22}\Gamma_{33}-\Gamma_{12}^2\Gamma_{33}-\Gamma_{13}^2\Gamma_{22}-\Gamma_{23}^2\Gamma_{11}\\ &\quad+\Gamma_{12}\Gamma_{23}\Gamma_{13}+\Gamma_{13}\Gamma_{12}\Gamma_{23},\\ a_1&=\Gamma_{22}\Gamma_{33}+\Gamma_{33}\Gamma_{11}+\Gamma_{11}\Gamma_{22}-\Gamma_{23}^2-\Gamma_{13}^2-\Gamma_{12}^2,\\ a_2&=\Gamma_{11}+\Gamma_{22}+\Gamma_{33},\end{aligned} \tag{38}$$

with

$$\begin{aligned}\Gamma_{11}&=p_{11}l_1^2+p_{66}l_2^2+p_{55}l_3^2,\\ \Gamma_{22}&=p_{66}l_1^2+p_{22}l_2^2+p_{44}l_3^2,\\ \Gamma_{33}&=p_{55}l_1^2+p_{44}l_2^2+p_{33}l_3^2,\\ \Gamma_{12}&=(p_{12}+p_{66})l_1l_2,\\ \Gamma_{13}&=(p_{13}+p_{55})l_3l_1,\\ \Gamma_{23}&=(p_{44}+p_{23})l_2l_3\end{aligned} \tag{39}$$

being the components of the Kelvin–Christoffel matrix (Carcione 2007).

In the (three) symmetry planes of an orthorhombic medium, there is a pure shear wave (labeled 1 below) and two coupled waves. The corresponding complex velocities are given by a generalization of the lossless case (e.g., Carcione 2007) to the lossy case: (x, y)-plane:

$$\begin{aligned}v_1&=\sqrt{(\rho)^{-1}(p_{55}l_1^2+p_{44}l_2^2)},\\ v_2&=(2\rho)^{-1/2}\sqrt{p_{11}l_1^2+p_{22}l_2^2+p_{66}-A},\\ v_3&=(2\rho)^{-1/2}\sqrt{p_{11}l_1^2+p_{22}l_2^2+p_{66}+A},\\ A&=\sqrt{[(p_{22}-p_{66})l_2^2-(p_{11}-p_{66})l_1^2]^2+4[(p_{12}+p_{66})l_1l_2]^2};\end{aligned} \tag{40}$$

(x, z)-plane:

$$\begin{aligned}v_1&=\sqrt{(\rho)^{-1}(p_{66}l_1^2+p_{44}l_3^2)},\\ v_2&=(2\rho)^{-1/2}\sqrt{p_{11}l_1^2+p_{33}l_3^2+p_{55}-A},\\ v_3&=(2\rho)^{-1/2}\sqrt{p_{11}l_1^2+p_{33}l_3^2+p_{55}+A},\\ A&=\sqrt{[(p_{33}-p_{55})l_3^2-(p_{11}-p_{55})l_1^2]^2+4[(p_{13}+p_{55})l_1l_3]^2};\end{aligned} \tag{41}$$

(y, z)-plane:

$$\begin{aligned}v_1&=\sqrt{(\rho)^{-1}(p_{66}l_2^2+p_{55}l_3^2)}\\ v_2&=(2\rho)^{-1/2}\sqrt{p_{22}l_2^2+p_{33}l_3^2+p_{44}-A},\\ v_3&=(2\rho)^{-1/2}\sqrt{p_{22}l_2^2+p_{33}l_3^2+p_{44}+A},\\ A&=\sqrt{[(p_{33}-p_{44})l_3^2-(p_{22}-p_{44})l_2^2]^2+4[(p_{23}+p_{44})l_2l_3]^2}.\end{aligned} \tag{42}$$

In terms of angles, $l_1=\sin\theta$ and $l_2=\cos\theta$ in the (x, y)-plane, $l_1=\sin\theta$ and $l_3=\cos\theta$ in the (x, z)-plane, and $l_2=\sin\theta$ and $l_3=\cos\theta$ in the (y, z)-plane.

The complex velocities along the principal axes are: (x, y)-plane:

$$\begin{aligned}v_1(0^\circ)&=v_{\mathrm{S}}(0^\circ)=\sqrt{p_{44}/\rho}\\ v_1(90^\circ)&=v_{\mathrm{S}}(90^\circ)=\sqrt{p_{55}/\rho}\\ v_2(0^\circ)&=v_{\mathrm{qS}}(0^\circ)=\sqrt{p_{66}/\rho}\\ v_2(90^\circ)&=v_{\mathrm{qS}}(90^\circ)=\sqrt{p_{66}/\rho}\\ v_3(0^\circ)&=v_{\mathrm{qP}}(0^\circ)=\sqrt{p_{22}/\rho}\\ v_3(90^\circ)&=v_{\mathrm{qP}}(90^\circ)=\sqrt{p_{11}/\rho};\end{aligned} \tag{43}$$

(x, z)-plane:

$$\begin{aligned}v_1(0^\circ)&=v_{\mathrm{S}}(0^\circ)=\sqrt{p_{44}/\rho}\\ v_1(90^\circ)&=v_{\mathrm{S}}(90^\circ)=\sqrt{p_{66}/\rho}\\ v_2(0^\circ)&=v_{\mathrm{qS}}(0^\circ)=\sqrt{p_{55}/\rho}\\ v_2(90^\circ)&=v_{\mathrm{qS}}(90^\circ)=\sqrt{p_{55}/\rho}\\ v_3(0^\circ)&=v_{\mathrm{qP}}(0^\circ)=\sqrt{p_{33}/\rho}\\ v_3(90^\circ)&=v_{\mathrm{qP}}(90^\circ)=\sqrt{p_{11}/\rho};\end{aligned} \tag{44}$$

(y, z)-plane:

$$\begin{aligned}
v_1(0^\circ) &= v_{\mathrm{S}}(0^\circ) = \sqrt{p_{66}/\rho}\\
v_1(90^\circ) &= v_{\mathrm{S}}(90^\circ) = \sqrt{p_{55}/\rho}\\
v_2(0^\circ) &= v_{\mathrm{qS}}(0^\circ) = \sqrt{p_{44}/\rho}\\
v_2(90^\circ) &= v_{\mathrm{qS}}(90^\circ) = \sqrt{p_{44}/\rho}\\
v_3(0^\circ) &= v_{\mathrm{qP}}(0^\circ) = \sqrt{p_{33}/\rho}\\
v_3(90^\circ) &= v_{\mathrm{qP}}(90^\circ) = \sqrt{p_{22}/\rho}.
\end{aligned} \tag{45}$$

The energy velocity can be computed for each frequency component, with the wavefront corresponding to the energy velocity at "infinite" frequency. Let us consider the (x, z)-plane of symmetry. The energy-velocity vector of the qP and qS waves is given by

$$\frac{\mathbf{v}_{\mathrm{e}}}{v_{\mathrm{p}}} = (l_1 + l_3 \cot\psi)^{-1}\hat{\mathbf{e}}_1 + (l_1 \tan\psi + l_3)^{-1}\hat{\mathbf{e}}_3 \tag{46}$$

(Carcione 2007; eq. 6.158), where

$$\tan\psi = \frac{\mathrm{Re}(\gamma^* X + \xi^* W)}{\mathrm{Re}(\gamma^* W + \xi^* Z)} \tag{47}$$

defines the angle between the energy-velocity vector and the z-axis,

$$\begin{aligned}
&\gamma = \sqrt{A \pm B},\\
&\xi = \pm \mathrm{pv}\sqrt{A \mp B},\\
&B = p_{11} l_1^2 - p_{33} l_3^2 + p_{55}\cos 2\theta,
\end{aligned} \tag{48}$$

where the upper and lower signs correspond to the qP and qS waves, respectively. Moreover,

$$\begin{aligned}
&W = p_{55}(\xi l_1 + \gamma l_3),\\
&X = \gamma p_{11} l_1 + \xi p_{13} l_3,\\
&Z = \gamma p_{13} l_1 + \xi p_{33} l_3
\end{aligned} \tag{49}$$

(Carcione 2007; Eqs. 6.121–6.123), where "pv" denotes the principal value, which has to be chosen according to established criteria.

On the other hand, the energy velocity of the SH wave is

$$\mathbf{v}_{\mathrm{e}} = \frac{v_{\mathrm{p}}}{\rho \mathrm{Re}(v)}\left[l_1 \mathrm{Re}\left(\frac{p_{66}}{v}\right)\hat{\mathbf{e}}_1 + l_3 \mathrm{Re}\left(\frac{p_{44}}{v}\right)\hat{\mathbf{e}}_3\right] \tag{50}$$

and

$$\tan\psi = \frac{\mathrm{Re}(p_{66}/v)}{\mathrm{Re}(p_{44}/v)}\tan\theta \tag{51}$$

(Carcione 2007; eq. 4.115).

In general, we have the property

$$v_{\mathrm{p}} = v_{\mathrm{e}}\cos(\psi - \theta), \tag{52}$$

where $v_{\mathrm{e}} = |\mathbf{v}_{\mathrm{e}}|$.

The quality factor expressions for each symmetry plane are similar to the equations obtained for the symmetry plane of the monoclinic medium. Along pure mode directions, we have

$$Q_{II} = \frac{\mathrm{Re}(p_{II})}{\mathrm{Im}(p_{II})}, \ I = 1, \ldots, 6. \tag{53}$$

The attenuation has a maximum for a given value of the specific viscosity. Let us consider, for instance, the P-wave and Eq. (19). A calculation yields

$$Q_{11}^{-1} = \frac{c_{11}\omega\eta_N}{\kappa_N(\kappa_N + c_{11}) + \omega^2\eta_N^2}. \tag{54}$$

This function has a maximum at

$$\omega\eta_N = \sqrt{\kappa_N(\kappa_N + c_{11})} \approx \kappa_N \tag{55}$$

if $\kappa_N \gg c_{11}$. On the other hand,

$$Q_{JJ}^{-1} = \frac{(c_{1J}^2/c_{JJ})\omega\eta_N}{(\kappa_N + c_{11})(\kappa_N + c_{11} - c_{1J}^2/c_{JJ}) + \omega^2\eta_N^2}, \ J = 2, 3, \tag{56}$$

with a maximum at

$$\omega\eta_N = \sqrt{(\kappa_N + c_{11})(\kappa_N + c_{11} - c_{1J}^2/c_{JJ})}. \tag{57}$$

The attenuation of the shear waves (the 44, 55, and 66 components) have similar expressions. Two different values of the viscosity may give the same value of the quality factor, although the phase velocities differ.

3.3 Transversely Isotropic Media

The analysis for the HTI medium follows as a particular case of one of the symmetry planes of the orthorhombic medium. One can use the exact velocity expressions or the following approximations:

$$\begin{aligned}
v_1^2 &= (c_{55}/\rho)(1 - \delta_H \sin^2\theta),\\
v_2^2 &= (c_{55}/\rho)(1 - \delta_H \cos^2 2\theta - (c_{55}/c_{11})\delta_N \sin^2 2\theta),\\
v_3^2 &= (c_{11}/\rho)\\
&\quad [1 - (c_{55}/c_{11})\delta_H \sin^2 2\theta - (1 - 2(c_{55}/c_{11})\delta_N \cos^2\theta)^2],
\end{aligned} \tag{58}$$

where θ is the angle between the wavenumber vector and the vertical direction. Similar approximations have been obtained by Schoenberg and Douma (1988) (their Eq. 26) for VTI media (horizontal fractures). Schoenberg and Douma (1988) have written those expressions in terms of the coefficients $\delta_N/(1 - \delta_N)$ and $\delta_H/(1 - \delta_H)$, instead of δ_N and δ_H, respectively, assuming $\delta_N \ll 1$ and $\delta_H \ll 1$. Without imposing these conditions, more accurate expressions are obtained by using δ_N and δ_H, as in Chichinina et al. (2009a, b).

4 Examples

We consider the TI background medium studied by Schoenberg and Helbig (1997), representing a typical shale,

$$\mathbf{C} = \rho \begin{pmatrix} 10 & 4 & 2.5 & 0 & 0 & 0 \\ 4 & 10 & 2.5 & 0 & 0 & 0 \\ 2.5 & 2.5 & 6 & 0 & 0 & 0 \\ 0 & 0 & 0 & 2 & 0 & 0 \\ 0 & 0 & 0 & 0 & 2 & 0 \\ 0 & 0 & 0 & 0 & 0 & 3 \end{pmatrix} \qquad (59)$$

(in MPa), where ρ = 2,300 kg/m^3, e.g., c_{11} = 23 GPa . We assume a frequency $f = \omega/(2\pi) = 50$ Hz and the low- and high-frequency limits for comparison.

First, we consider two orthogonal sets of fractures with $\beta_1 = 0°$ and $\beta_2 = 90°$. The fracture stiffnesses of the first set are given by $\kappa_N^{(1)} = 9c_{11}$, $\kappa_H^{(1)} = \frac{8}{3}c_{66}$, and $k_V^{(1)} = 4c_{55}$. In the lossless case, we obtain $\delta_N^{(1)} = 0.1$, $\delta_H^{(1)} = 3/11$, and $\delta_V^{(1)} = 1/5$, i.e., the values used by Schoenberg and Helbig (1997). Moreover, we set $\kappa_N^{(2)} = b\kappa_N^{(1)}$, $\kappa_H^{(2)} = b\kappa_H^{(1)}$ and $k_V^{(2)} = bk_V^{(1)}$, with $b = 0.5$. The fracture viscosities are assumed to be $\eta_N^{(q)} = a\kappa_N^{(q)}$, $\eta_H^{(q)} = a\kappa_H^{(q)}$, and $\eta_V^{(q)} = ak_V^{(q)}$, where $a = 10^{-3}$ s, for both fracture sets. The stiffness-matrix components, given by Eq. (19), are

$$\begin{aligned} &p_{11} = (20.34, 0.70), && p_{12} = (6.93, 0.56), \\ &p_{13} = (4.87, 0.22), && p_{22} = (18.83, 1.05), \\ &p_{23} = (4.60, 0.29), && p_{33} = (13.44, 0.09), \\ &p_{44} = (3.13, 0.31), && p_{55} = (3.73, 0.22), \\ &p_{66} = (3.32, 0.53), && \end{aligned} \qquad (60)$$

in GPa. Figure 2 shows the dissipation factors as a function of frequency along pure mode directions. The attenuation behaves as relaxation peaks, similar to the Zener model. Figure 3 shows the energy velocity at the (x, z)-plane for 0 Hz (a), 50 Hz (b), and "infinite" frequency (c). The high-frequency limit corresponds to the unfractured TI case. The dissipation factors versus phase and ray angle are represented in Figure 4, where the pure mode (the SH wave) shows more attenuation. The attenuation of the coupled waves have a different behavior versus the ray angle, corresponding to the propagation of wave packets, compared to the representation versus the phase (propagation) angle, corresponding to the propagation of plane waves. In particular, the triplication appears also in the Q factor of the qS wave. Experimental setups should consider these facts.

Next, we consider two sets of fractures with $\beta_1 = 20°$ and $\beta_2 = 65°$ and perform the analysis in the symmetry axis of the effective monoclinic medium. The fracture parameters corresponding to the first example are considered. The stiffness-matrix components, given by Eq. (15), are

$$\begin{aligned} &p_{11} = (18.05, 1.1), && p_{12} = (8.98, 0.29), \\ &p_{13} = (4.83, 0.23), && p_{16} = (-1.07, 0.13), \\ &p_{22} = (17.27, 1.26), && p_{23} = (4.69, 0.26), \\ &p_{26} = (-0.15, 0.05), && p_{33} = (13.44, 0.09), \\ &p_{36} = (-0.22, 0.03), && p_{44} = (3.37, 0.25), \\ &p_{45} = (-0.67, 0.11), && p_{55} = (3.70, 0.19), \\ &p_{66} = (4.53, 0.46), && \end{aligned} \qquad (61)$$

in GPa. Figure 5 shows the low-frequency limit energy velocities (a) and dissipation factors (b) in the (x, y) symmetry plane as a function of the phase (propagation) angle. The frequency in Fig. 5b is f = 50 Hz. In this case, the qS wave shows the maximum attenuation.

In order to verify the shape of the wavefronts shown in Fig. 5, we perform a 2D full-wave numerical simulation of qP–qS propagation in the symmetry plane, where the effective medium is defined by the low-frequency elasticity

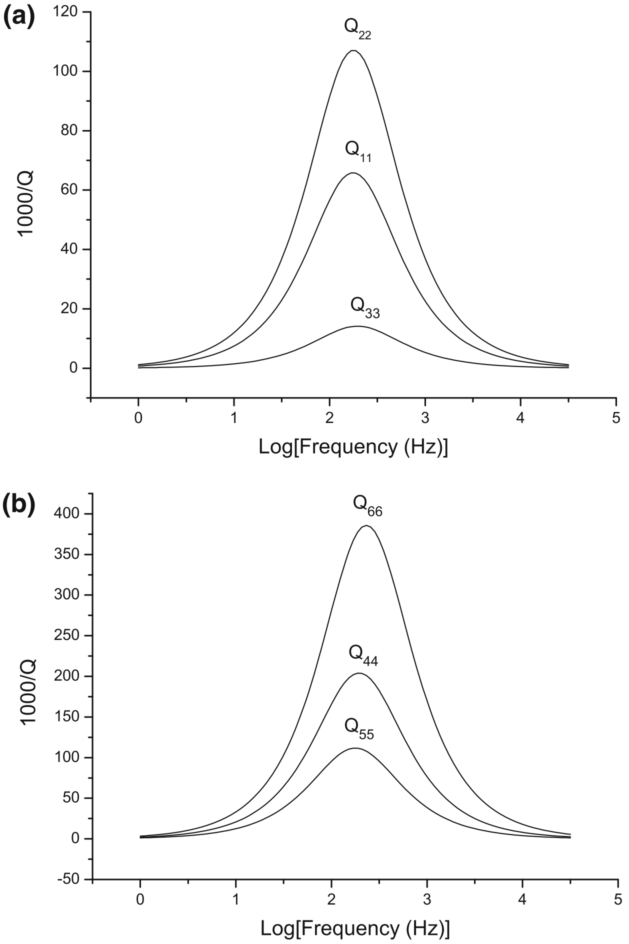

Fig. 2 Dissipation factors (53) as a function of frequency, where (**a**) corresponds to the P waves and (**b**) corresponds to the S waves

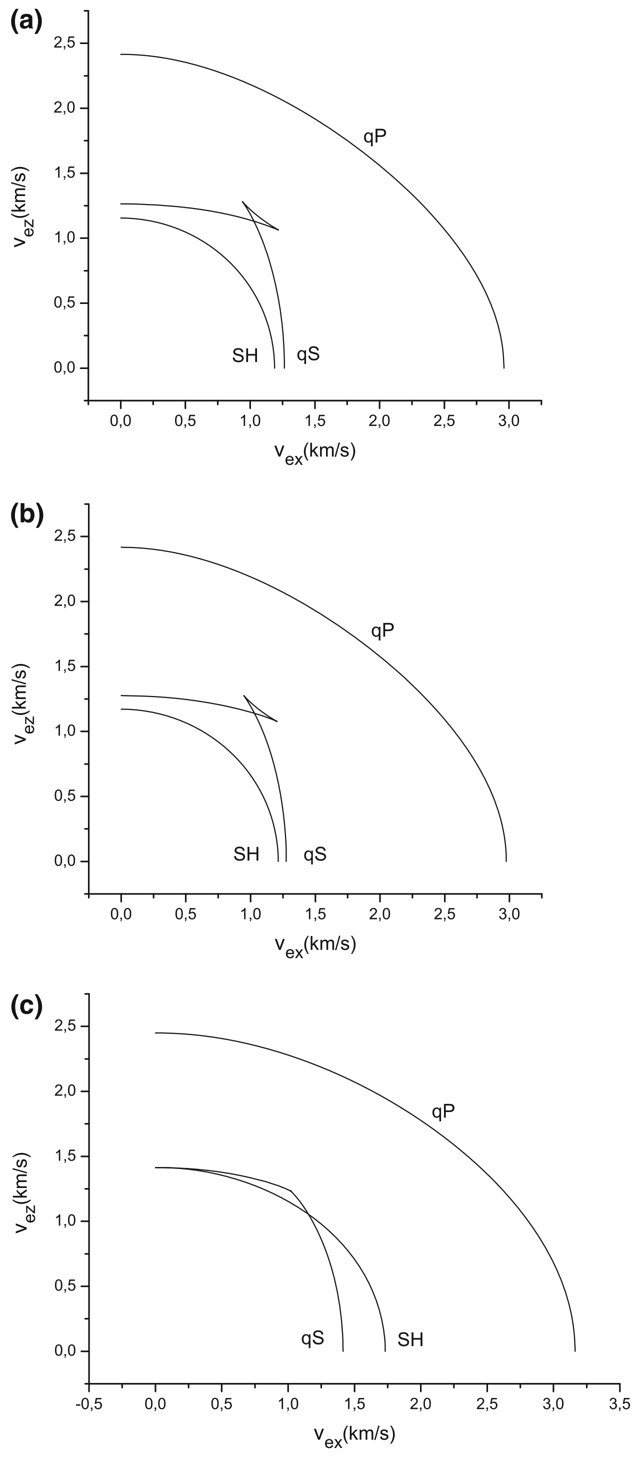

Fig. 3 Energy velocities in the (x, z) symmetry plane of the equivalent orthorhombic medium, where (**a**) f = 0 Hz, (**b**) f = 50 Hz, and (**c**) $f = \infty$ Hz

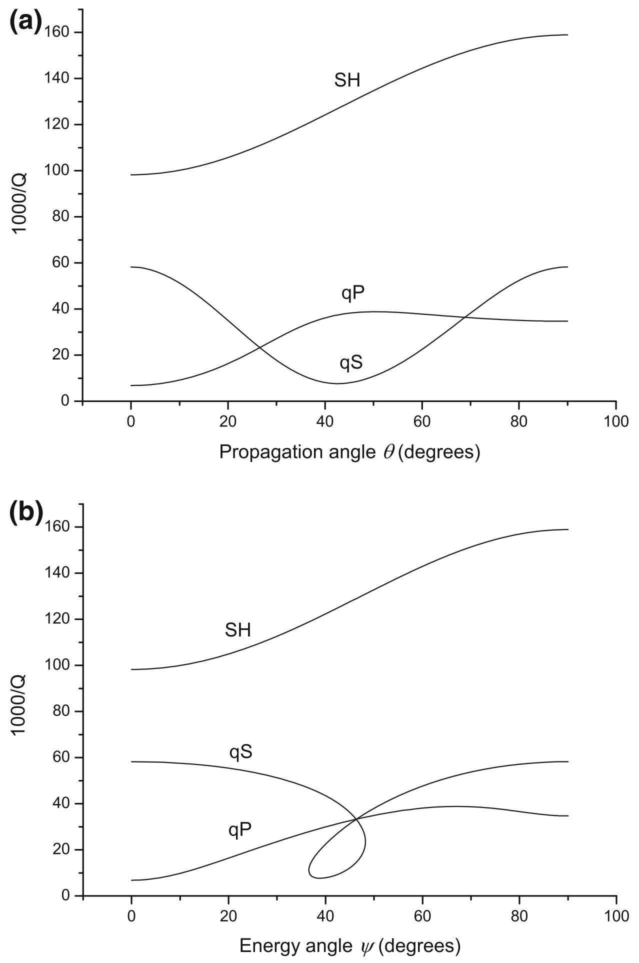

Fig. 4 Quality factors in the (x, z) symmetry plane as a function of the phase (propagation) angle (**a**) and ray (energy) angle (**b**). The equivalent medium has orthorhombic symmetry and the frequency is f = 50 Hz

constants: c_{11}^0 = 17.8 GPa, c_{22}^0 = 17 GPa, c_{12}^0 = 8.9 GPa, c_{16}^0 = −1.08 GPa, c_{26}^0 = −0.16 GPa, and c_{66}^0 = 4.44 GPa. The density is ρ = 2,300 kg/m^3. The algorithm solves the particle-velocity/stress formulation based on the Fourier pseudospectral method for computing the spatial derivatives and a 4th-order Runge–Kutta technique for calculating the wavefield recursively over time (e.g., Carcione 2007). The source is a vertical force with a Ricker time history, located at the center of the mesh. The simulation uses a 455 × 455 mesh with 1-m grid spacing and the central frequency of the source is 80 Hz. The algorithm has a time step of 0.1 ms and a snapshot of the vertical-particle velocity is computed at 80 ms (see Fig. 6). It is verified that the results of the modeling algorithm and plane-wave analysis are in agreement.

Finally, we test the approximation

$$Q^{-1}(\theta) \approx Q_{\mathrm{b}}^{-1}(\theta) + Q_{\mathrm{f}}^{-1}(\theta), \qquad (62)$$

where Q_{b} and Q_{f} are the quality factors of the background medium and fracture set in the same lossless background medium, respectively. Equation (62) is commonly used in the literature to obtain the total quality factor due to different attenuation mechanisms (e.g., Chichinina et al. 2009a, b). We assume for simplicity an isotropic

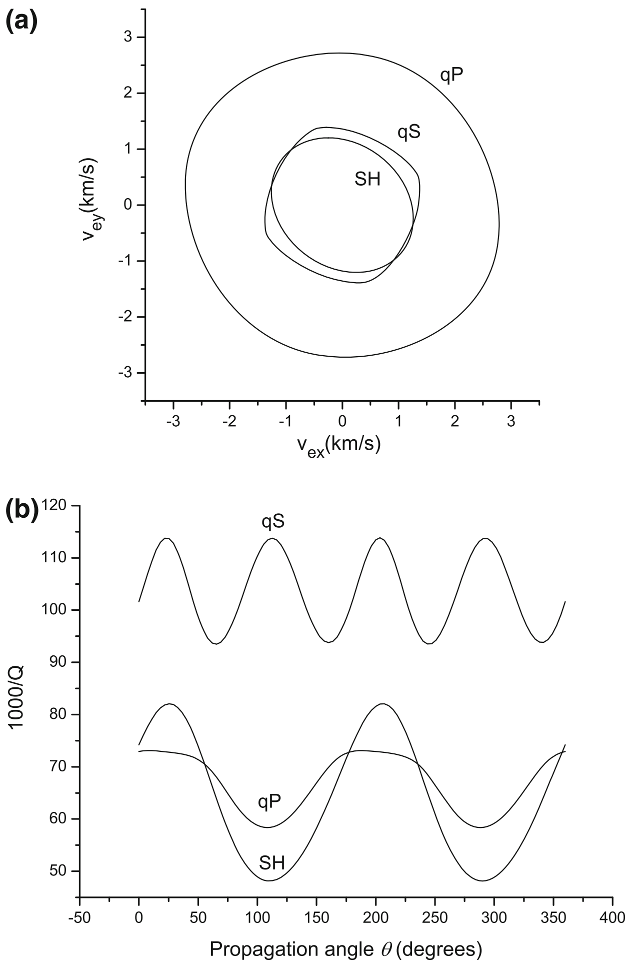

Fig. 5 Low-frequency limit energy velocities (**a**) and dissipation factors (**b**) in the (x, y) symmetry plane as a function of the phase (propagation) angle. The equivalent medium has monoclinic symmetry and the frequency in **b** is $f = 50$ Hz

background medium, and, therefore, Q_b is independent of θ. The effective medium has HTI symmetry and the stiffness matrix is given by Eq. (22), with c_{IJ} complex. Let us consider the simplest model, i.e., $c_{11} \rightarrow c_{11}(Q_P + i)$ and $c_{55} \rightarrow c_{55}(Q_S + i)$, where Q_P and Q_S are the P-wave and S-wave quality factors of the background medium. (Note that $c_{12} = c_{11} - 2c_{55}$.) Let us assume that $Q_P = 20$ and $Q_S = 15$. Figure 7 compares the exact dissipation factors to the approximate dissipation factors, corresponding to the qP and qS waves, respectively. As can be appreciated, Eq. (62) is a rough approximation and should be used with caution. The approximation improves if Q increases.

In order to verify that the equivalent-medium theory of fractures is correct, we consider an isotropic background medium defined by $c_{12} = 10$ GPa, $c_{55} = 3.9$ GPa, and $\rho = 2{,}300$ kg/m^3 containing a horizontal and plane fracture set defined by $\kappa_1 = 15{,}500$ GPa/m and $\eta_1 = 36$ GPa s/m (tangential stiffnesses per unit length), and $\kappa_3 = 34{,}000$ GPa/m and $\eta_3 = 80$ GPa s/m (normal stiffnesses per unit length). The fracture planes are parallel to the (x, y)-plane and perpendicular to the z-axis. The novel methodology consists of applying time-harmonic oscillatory tests at a finite number of frequencies. Each test is based on the wave equation of motion expressed in the space–frequency domain, implementing explicitly the fracture boundary conditions, and solved with a finite-element method. A similar algorithm considering multiple thin layers is given by Santos et al. (2011). Figure 8 shows the phase velocity v_p (a) and dissipation factor 1,000 Q^{-1} along the horizontal direction (component 11, circles) and vertical direction

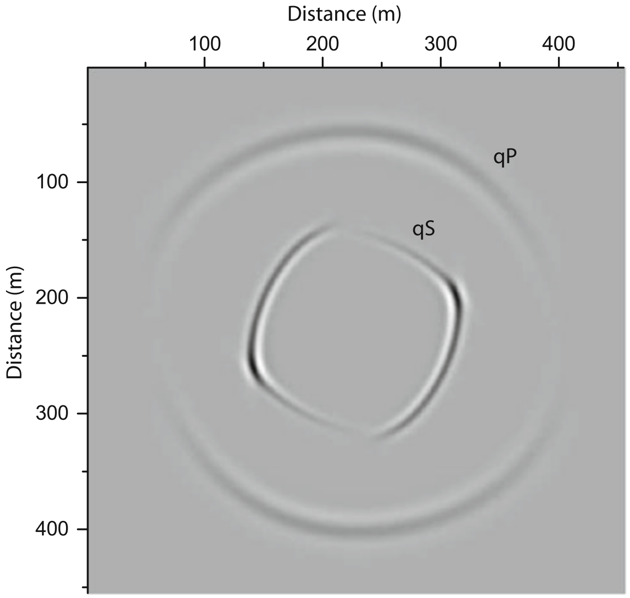

Fig. 6 Snapshot in the (x, y) symmetry plane of the monoclinic effective medium. The elasticity constants are those of the low-frequency limit

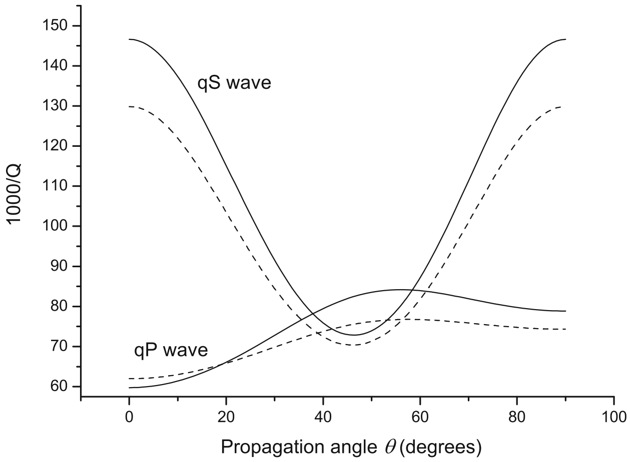

Fig. 7 Exact (*solid lines*) and approximate (*dashed lines*) dissipation factors of the qP and qS waves as a function of the propagation angle. The frequency is 50 Hz

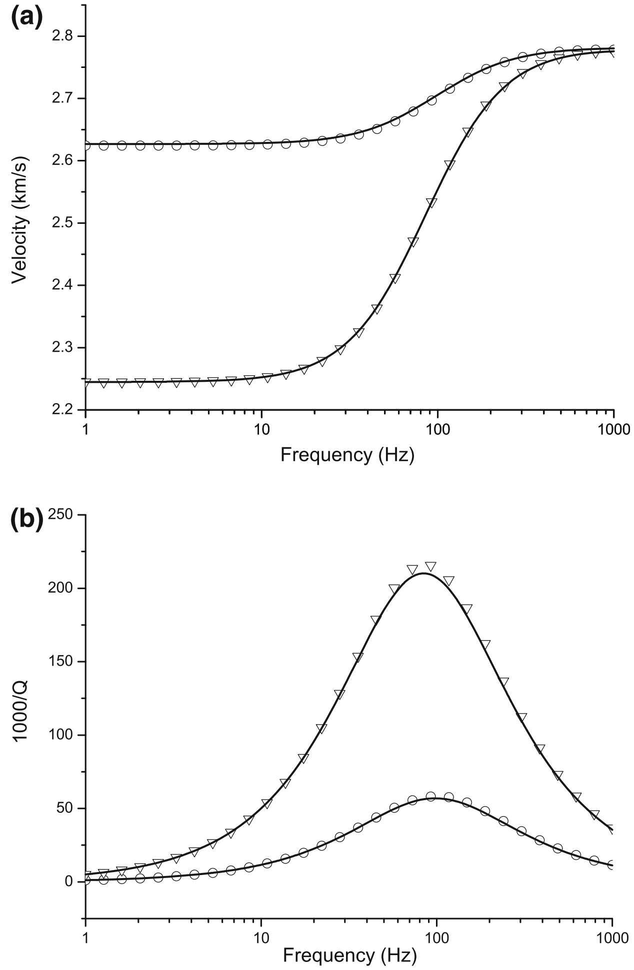

Fig. 8 Numerical phase velocity (**a**) and dissipation factor (**b**) along the horizontal direction (*circles*) and vertical direction (*triangles*) corresponding to a fracture set embedded in a homogeneous and isotropic medium. The *solid lines* correspond to the theoretical curves

(component 33, triangles). The match between the theory (solid lines) and numerical results is very good.

5 Conclusions

We have presented a theory to obtain the wave velocities and attenuation of many sets of vertical fractures embedded in a transversely isotropic medium. The anisotropic effective medium has monoclinic symmetry. Fractures are modeled as boundary discontinuities in the displacement and particle velocity fields. The theory generalizes an existing model describing the acoustic properties of a single set of fractures embedded in an isotropic background medium. The expressions of the complex and frequency-dependent stiffness constants corresponding to two orthogonal sets of fractures are obtained explicitly, where the effective medium has orthorhombic symmetry. The phase, energy, and quality factors as a function of the propagation and ray (energy) angle are obtained for homogeneous viscoelastic plane waves (wavenumber and attenuation directions coincide). We consider the symmetry plane of a monoclinic medium and the three symmetry planes of an orthorhombic medium. The examples show that the effective media have high anisotropy and show relaxation attenuation peaks, similar to Zener viscoelastic models. Moreover, we have tested the commonly used equation stating that the dissipation factor of the effective medium is equal to the sum of the dissipation factors of the background medium and fractured background (lossless) medium. The results indicated that this equation is not a good approximation for realistic *Q* values of the background medium. Finally, we performed a cross-check of the theory with the computations of a finite-element algorithm, showing that both phase velocity and dissipation factors agree with the numerical results.

The novel model can be important in determining the orientation of fractures in the reservoir and the overlying cap rock. This plays an important role during production and other applications, such as CO_2 injection and monitoring.

References

Backus GE (1962) Long-wave elastic anisotropy produced by horizontal layering. J Geophys Res 67:4427–4440

Barton N (2007) Fracture-induced seismic anisotropy when shearing is involved in production from fractured reservoirs. J Seism Explor 16:115–143

Carcione JM (1992) Anisotropic *Q* and velocity dispersion of finely layered media. Geophys Prospect 40:761–783

Carcione JM (1996a) Plane-layered models for the analysis of wave propagation in reservoir environments. Geophys Prospect 44:3–26

Carcione JM (1996b) Elastodynamics of a non-ideal interface: application to crack and fracture scattering. J Geophys Res 101:28177–28188

Carcione JM (2007) Wave fields in real media: wave propagation in anisotropic, anelastic, porous and electromagnetic media. In: Handbook of geophysical exploration (revised and extended), vol 38, 2nd edn. Elsevier, Amsterdam, pp 321–383

Carcione JM, Cavallini F (1994) A rheological model for anelastic anisotropic media with applications to seismic wave propagation. Geophys J Int 119:338–348

Carcione JM, Cavallini F, Helbig K (1998) Anisotropic attenuation and material symmetry. Acustica 84:495–502

Carcione JM, Santos JE, Picotti P (2011) Anisotropic poroelasticity and wave-induced fluid flow: harmonic finite-element simulations. Geophys J Int 186:1245–1254

Chapman M (2003) Frequency-dependent anisotropy due to meso-scale fractures in the presence of equant porosity. Geophys Prospect 51:369–379

Chichinina TI, Obolentseva IR, Ronquillo-Jarillo G (2009a) Anisotropy of seismic attenuation in fractured media: theory and ultrasonic experiment. Transp Porous Media 79:1–14

Chichinina TI, Obolentseva IR, Gik L, Bobrov B, Ronquillo-Jarillo G (2009b) Attenuation anisotropy in the linear-slip model: interpretation of physical modeling data. Geophysics 74:WB165–WB176

Coates RT, Schoenberg M (1995). Finite-difference modeling of faults and fractures. Geophysics 60:1514–1526

Fan LF, Ren F, Ma GW (2011) An extended displacement discontinuity method for analysis of stress wave propagation in viscoelastic rock mass. J Rock Mech Geotech Eng 3:73−81

Grechka VA, Bakulin A, Tsvankin I (2003) Seismic characterization of vertical fractures described as general linear-slip interfaces. Geophys Prospect 51:117–130

Grechka V, Tsvankin I (2003) Feasibility of seismic characterization of multiple fracture sets. Geophysics 68:1399–1407

Hall SA, Kendall J-M (2003) Fracture characterization at Valhall: application of P-wave amplitude variation with offset and azimuth (AVOA) analysis to a 3D ocean-bottom data set. Geophysics 68:1150–1160

Hansen BRH (2002) Evaluating the impact of fracture-induced anisotropy on reservoir rock property estimates made from seismic data. Report no.: GPH 7/02, Curtin University of Technology

Hood JA (1991) A simple method for decomposing fracture-induced anisotropy. Geophysics 56:1275–1279

Krzikalla F, Müller T (2011) Anisotropic P-SV-wave dispersion and attenuation due to inter-layer flow in thinly layered porous rocks. Geophysics 76:WA135–WA145. doi:10.1190/1.3555077

Liu E, Hudson JA, Pointer T (2000) Equivalent medium representation of fractured rock. J Geophys Res 105:2981–3000

Maultzsch S (2005) Analysis of frequency-dependent anisotropy in VSP data. PhD thesis, University of Edinburgh

Nakagawa S, Myer LR (2009) Fracture permeability and seismic wave scattering—poroelastic linear-slip interface model for heterogeneous fractures. SEG Expanded Abstracts 28, 3461. doi: 10.1190/1.3255581

Nichols D, Muir F, Schoenberg M (1989) Elastic properties of rocks with multiple sets of fractures. In: Proceedings of the 63rd Annual International Meeting of the Society of Exploration Geophysicists, Extended Abstracts, pp 471–474

Perino A, Zhu, JB, Li JC, Barla G, Zhao J (2010) Theoretical methods for wave propagation across jointed rock masses. Rock Mech Rock Eng 43:799–809

Picotti S, Carcione JM, Santos JE, Gei D (2010) *Q*-anisotropy in finely layered media. Geophys Res Lett 37:L06302.1–L06302.6. doi:10.1029/2009GL042046

Pyrak-Nolte LJ, Myer LR, Cook NGW (1990) Transmission of seismic waves across single natural fractures. J Geophys Res 95:8617–8638

Santos JE, Carcione JM, Picotti S (2011) Viscoelastic-stiffness tensor of anisotropic media from oscillatory numerical experiments. Comput Methods Appl Mech Eng 200:896–904

Schoenberg M (1980) Elastic wave behavior across linear slip interfaces. J Acoust Soc Am 68:1516–1521

Schoenberg M (1983) Reflection of elastic waves from periodically stratified media with interfacial slip. Geophys Prospect 31:265–292

Schoenberg M, Douma J (1988) Elastic wave propagation in media with parallel fractures and aligned cracks. Geophys Prospect 36:571–590

Schoenberg M, Helbig K (1997) Orthorhombic media: modeling elastic wave behavior in a vertically fractured earth. Geophysics 62:1954–1974

Schoenberg M, Muir F (1989) A calculus for finely layered anisotropic media. Geophysics 54:581–589

Schoenberg M, Dean S, Sayers C (1999) Azimuth-dependent tuning of seismic waves reflected from fractured reservoirs. Geophysics 64:1160–1171

Zhang J, Gao H (2009) Elastic wave modelling in 3-D fractured media: an explicit approach. Geophys J Int 177:1233–1241

Zhu Y, Tsvankin I (2007) Plane-wave attenuation anisotropy in orthorhombic media. Geophysics 72:D9–D19